European Journal of Chemistry

View Journal Online
View Article Online

Solubility enhancement and structural insights into pipemidic acid via salt formation with benzoic acid

Shwetha Jayapura Chandrashekar [1], Rajalakshmanan Eswaramoorthy [2] and Kamalakaran Anand Solomon [3,*]

[1] *Department of Physical and Chemical Science, Sri Sathya Sai University for Human Excellence, Navanihal, Kalaburagi, 585313, Karnataka, India*
[2] *Centre of Molecular Medicine and Diagnostics, Department of Biochemistry, Saveetha Dental College and Hospital, Saveetha Institute of Medical and Technical Sciences, 600077, Chennai, India*
[3] *Department of Chemistry, School of Engineering, Dayananda Sagar University, Devarakaggalahalli, Harohalli, Kanakapura Road, Dt, Ramanagara, 562112, Karnataka, India*

* *Corresponding author at: Department of Chemistry, School of Engineering, Dayananda Sagar University, Devarakaggalahalli, Harohalli, Kanakapura Road, Dt, Ramanagara, 562112, Karnataka, India.*
e-mail: anand.dcb@gmail.com (K.A. Solomon).

RESEARCH ARTICLE

10.5155/eurjchem.16.2.104-116.2631

Received: 06 January 2025
Received in revised form: 26 March 2025
Accepted: 23 April 2025
Published online: 30 June 2025
Printed: 30 June 2025

KEYWORDS

Solubility
Benzoic acid
Pipimedic acid
Dissolution rate
Hirshfeld surface analysis
Single-crystal X-ray diffraction

ABSTRACT

Pipemidic acid (PMA) is an active pharmaceutical ingredient (API) belonging to the quinolone class of antibacterial agents, primarily used to treat urinary tract infections. This study investigated improving the dissolution properties of poorly soluble PMA by forming a 1:1 stoichiometry molecular salt (4BA) with benzoic acid (BA). Liquid-assisted grinding and slow evaporation techniques were used to prepare the solid form of the salt. The salt was then characterized using differential scanning calorimetry (DSC), Fourier transform infrared spectroscopy (FTIR), and single-crystal X-ray diffraction (SC-XRD). The DSC analysis provided information on the changes in thermal behavior associated with the formation of the salt. FTIR spectroscopy helped identify the functional groups present and potential interactions between PMA and benzoic acid. SC-XRD determined the definitive three-dimensional arrangement of atoms within the salt structure, revealing a wave-like hydrogen bonding network directing a 3D layered packing of molecules. This improved packing is believed to be responsible for the improved solubility of PMA in the salt form. The Hirshfeld surface analysis, along with its associated 2D fingerprint plots, further elucidated the intermolecular interactions within the crystal lattice. This analysis showed that, in addition to the strong N-H···O and O-H···O hydrogen bonds, weaker H···H, C···H, and H···C interactions also play a significant role in stabilizing the molecular packing. Finally, cumulative drug release (CDR) showed that the formation of the molecular salt significantly improved the dissolution behavior of PMA, potentially leading to sustained drug release.

Cite this: *Eur. J. Chem.* **2025**, *16(2)*, 104-116 **Journal website**: www.eurjchem.com

1. Introduction

Pipimedic acid (PMA), a synthetic antibacterial agent belonging to the class of quinolones, is used primarily to treat urinary tract infections [1]. PMA's antimicrobial activity works by inhibiting the enzymes DNA gyrase and topoisomerase IV, which are essential for the replication and repair of bacterial DNA [2]. This inhibition halts bacterial growth and proliferation, helping to resolve infections [3]. However, its solubility in water limits its absorption in the gastrointestinal tract, leading to suboptimal therapeutic levels in the body.

Benzoic acid (BA), a simple aromatic carboxylic acid, has been widely used in pharmaceutical formulations due to its solubilizing properties and compatibility with various drugs [4]. The carboxylic acid group in BA can interact with the amine group in PMA, leading to the formation of a stable salt [5]. This interaction can result in significant changes in the physico-chemical properties of PMA, including its solubility, dissolution rate, and stability [6].

The improvement of PMA solubility through the formation of BA salts aims to overcome limitations and improve its clinical efficacy [7]. Previous studies have demonstrated the potential of salt formation to improve the solubility and bioavailability of quinolone antibiotics [8], making this approach particularly relevant for PMA. The enhancement of PMA through the formation with BA is expected to improve its bioavailability, thereby enhancing its therapeutic efficacy. Improved solubility can lead to better absorption of the drug in the gastrointestinal tract, resulting in higher plasma concentrations and improved clinical outcomes [9].

Molecular salt formation involves the interaction between an ionizable drug and a suitable counterion to form a salt [10]. This process can significantly improve the solubility, stability, and bioavailability of drugs [11]. The choice of counterion is critical in salt formation, as it can influence the physicochemical properties and pharmacokinetic profile of the resulting salt [12].

ISSN 2153-2249 (Print) / ISSN 2153-2257 (Online) – Copyright © 2025 The Authors – Atlanta Publishing House LLC – Printed in the USA.
This work is published and licensed by Atlanta Publishing House LLC – CC BY NC – Some Rights Reserved.
https://dx.doi.org/10.5155/eurjchem.16.2.104-116.2631

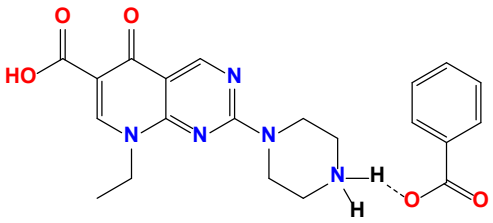

Figure 1. Molecular structure of 4BA.

BA, a commonly used pharmaceutical excipient, was chosen in this study as the counterion for salt formation with PMA. BA is known for its safety, low toxicity, and ability to enhance the solubility of various drugs through salt formation [13].

The structural characterization of the newly formed salt is essential to understand these changes and their impact on drug properties. Techniques such as X-ray diffraction (XRD), Fourier transform infrared spectroscopy (FTIR), differential scanning calorimetry (DSC) are commonly employed for this purpose [14]. These techniques provide insight into the crystal structure, thermal behavior, and molecular interactions within the salt, facilitating the optimization of its pharmacokinetic and pharmacodynamic properties [15].

The formation of a new crystalline lattice arises from noncovalent interactions between the active pharmaceutical ingredient (API) and the conformer, giving the structure unique properties [16]. These interactions, such as hydrogen bonding, π-π stacking, and other weak forces, are fundamental in shaping the structure and behavior of the molecular salt [17]. As a result, molecular salts often exhibit different characteristics from the pure API, including improved solubility, faster dissolution rates [18], altered melting points, greater stability, and enhanced mechanical properties [19], which can be highly beneficial for pharmaceutical applications [20]. Furthermore, structural characterization offers important information on these transformations of PMA through the formation of molecular salts (Figure 1) with BA.

2. Experimental

2.1 Materials

For this study, materials were obtained from commercial suppliers in India. PMA (CAS No. 51940-44-4), with a purity level of at least 99%, was purchased from Yarrow Chem Products in Mumbai. The conformer and organic solvents, all classified as HPLC grade, were acquired from Lab Reagents and Allied Products in Bengaluru. In addition, HPLC-grade solvents, including methanol and phosphate buffered saline (PBS), were also obtained from the same supplier in Bengaluru.

2.2. Preparation and growth of molecular salts 4BA

A molecular salt, 4BA, was prepared by dissolving 0.244 g of benzoic acid and 0.050 g of PMA in a 1:1 mixture of methanol and water. The resulting solution was heated to 90 °C and allowed to evaporate slowly in a 20 mL beaker. After five days, rod-shaped crystals with a light brown hue were observed to have formed.

2.3. Preparation of the calibration curve

An accurate weight of 200 mg PMA was transferred to a 100 mL volumetric flask, where it was dissolved and diluted with a 1:1 ethanol: water mixture until the mark, resulting in a stock solution with a concentration of 1000 µg/mL. Subsequently, a working standard solution of 100 µg/mL was prepared by diluting 1 mL of the stock solution to 10 mL with phosphate buffer saline (PBS). Various volumes (1, 2, 3, 4, 5, 6, 7, 8, 9, 10, 11, 12 and 13 mL) of the standard stock solution of PMA were pipetted into a series of 100 mL volumetric flasks. Each flask was then filled up to 100 mL with 1:1 ethanol: water mixture to obtain solutions with concentrations of 10, 20, 30, 40, 50, 60, 70, 80, 90, 100, 110, 120, and 130 µg/mL of the drug. The calibration curve was constructed using the absorbance measured at 280 nm for standards containing 2-30 µg/mL of PMA.

2.4. Antimicrobial activity

To determine the antimicrobial efficacy of PMA salts, the microbroth dilution technique [21] was used. In Mueller Hinton broth (MHB), the compounds were serially diluted from 256 to 4 µg. In the appropriate wells, the bacterial culture was added after being adjusted to 0.5 MC Farland. The plates were incubated at 37 °C for 16-18 hours.

2.4.1. Biofilm assay

The overnight culture was diluted to a 1:100 ratio and aliquoted to the wells. After one hour, the compound was added at the desired concentration and the wells were allowed to incubate for 16-18 hours. Without disturbing the biofilm, the medium was removed and washed with sterile water. The biofilms were stained for 15 minutes with 0.1% crystal violet. The stain was removed, cleaned with water, and allowed to air dry. The Tecan infinite F_{50} plate reader was used to measure the absorbance after the plates were destained with 30% acetic acid.

2.5. Characterization

Fourier transform infrared spectroscopy (FT-IR), differential scanning calorimetry (DSC), and single-crystal X-ray diffraction (SCXRD) were employed to analyze PMA and its salts. The infrared spectra of PMA and its binary solids were recorded using a Thermo Nicolet 6700 FTIR spectrometer (Thermo Scientific, Waltham, MA) by dispersing the samples in KBr pellets and scanning them over a spectral range of 4000 to 400 cm^{-1}. Data were processed using Spectrum software version 2 (JASCO, Easton, Maryland, USA). For thermal analysis, a Mettler Toledo DSC instrument (model no DSC00f3MAYA) was used to study the thermal properties of PMA and its salts, the samples being placed in aluminum pans under nitrogen purging. Single crystal X-ray diffraction (SC-XRD) analysis of the 4BA salt was performed using a Bruker AXS KAPPA APEX-II CCD diffractometer with MoKα radiation at 296 K (Figure 2). The structure was refined using the salt SHELX program [22], and the structure was modeled using the Olex2 program [23]. Atom site locations were identified through the structure invariant direct method and the difference Fourier map. The crystal data and processing details are provided in Table 1 and 2, and full structural parameters are available in CIF format from the Cambridge Crystallographic Data Centre (CCDC 2168989 for 4BA).

Table 1. Crystal data and structure refinement for the 4BA.

Empirical formula	$C_{49}H_{53}N_{10}O_{13}$
Formula weight (g/mol)	990.01
Temperature (K)	296(2)
Crystal system	Triclinic
Space group	*P*-1
a, (Å)	10.4629(10)
b, (Å)	14.4930(15)
c, (Å)	17.3127(18)
α (°)	77.910(5)
β (°)	78.781(5)
γ (°)	76.558(4)
Volume (Å^3)	2467.2(4)
Z	2
ρ_{calc} (g/cm^3)	1.333
μ (mm^{-1})	0.098
F(000)	1042.0
Crystal size (mm^3)	0.4 × 0.35 × 0.3
Radiation	MoKα (λ = 0.71073)
2Θ range for data collection (°)	2.434 to 57.592
Index ranges	$-10 \le h \le 14$, $-19 \le k \le 19$, $-23 \le l \le 22$
Reflections collected	30449
Independent reflections	12429 [R_{int} = 0.0394, R_{sigma} = 0.0624]
Data/restraints/parameters	12429/3/662
Goodness-of-fit on F^2	1.022
Final R indexes [I≥2σ (I)]	R_1 = 0.0773, wR_2 = 0.2337
Final R indexes [all data]	R_1 = 0.1633, wR_2 = 0.3049
Largest diff. peak/hole (e.Å^{-3})	0.89/-0.39
CCDC Numbers	2168989

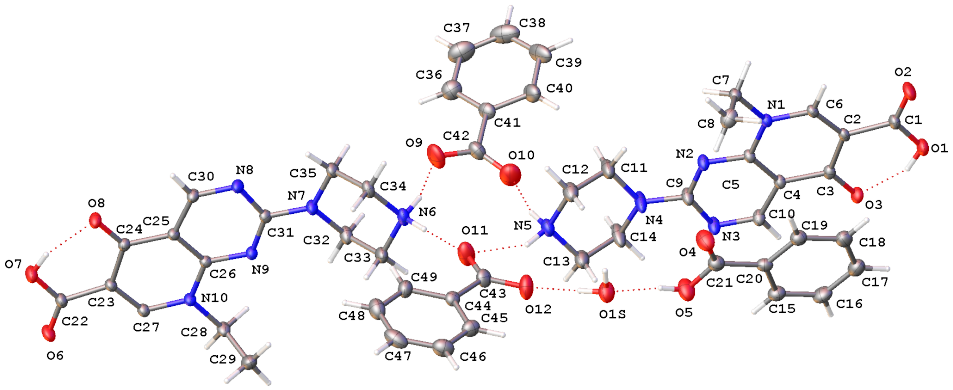

Figure 2. Molecular structure of 4BA, showing the atom labeling scheme.

2.6. Computational analysis

To analyze the Hirshfeld surface of the organic salt under study, Crystal Explorer 17.5 software was used [24]. For calculating the HOMO-LUMO energy levels, the density functional theory (DFT) method was applied using the B3LYP/6-31G(d,p) geometry [25,26] and converted from the CIF format to the MOL2 format using Mercury 4.0 software [27]. After importing, the structure was optimized using Gaussian's geometry optimization algorithm. Once the optimized structure was obtained, energy calculations were performed to determine the frontier molecular orbitals (HOMO and LUMO), the total molecular energy, and the dipole moment. The visualization of these orbitals was also generated during this step. Additionally, a molecular electrostatic potential (MEP) map was created using the contour builder feature in GaussView 6 [28].

3. Results and discussion

3.1. FT-IR analysis

FTIR is commonly utilized to characterize interactions within molecular salts, enabling differentiation between salts and molecular salts. When a molecular salt forms, the hydrogen bonding patterns within the molecule alter, leading to shifts in the vibrational modes of functional groups and the corresponding changes in the IR frequencies [29]. The IR spectrum of PMA exhibited a moderate peak at 1620 cm^{-1} for the carboxylic carbonyl (C=O) stretching and a band at 1640 cm^{-1} for the ring carbonyl (ketone) group. Furthermore, the O-H stretching appeared as a moderate absorption peak at 3460 cm^{-1} [30,31]. The FT-IR of BA showed characteristic features such as the broad peak of the acidic OH stretch spanning from 3071 cm^{-1} to approximately 2940 cm^{-1}, and the prominent C=O stretch observed at 1684 cm^{-1}. Additional bands specific to this aromatic carboxylic acid compound are also evident [32]. In particular, upon the formation of 4BA, the absence of the acidic OH stretch at 3071 cm^{-1} suggests the formation of a molecular salt between the carboxylate group and PMA. This interpretation is further supported by the significant reduction in intensity of the C=O stretching peak at 1684 cm^{-1}. The C-O and O-H peaks of BA around 1292 and 934 cm^{-1} shifts to lower wavenumbers (1280 and 916 cm^{-1}) and become less intense in 4BA. The spectral changes suggest the formation of a molecular salt between the carboxylate group (from BA) and PMA in 4BA. Table 3 presents the FT-IR stretching frequencies for various functional groups, including COOH, COO-, NH / OH and aliphatic and aromatic CH peaks, observed in PMA and its molecular salts. These frequencies provide important insights into the molecular interactions and structural changes that occur in the salts in comparison to those occurring in the parent PMA compound.

Table 2. Bond lengths (Å) and angles (°) for 4BA.

Atom	Atom	Length	Atom	Atom	Length	Atom	Atom	Length	Atom	Atom	Length
C1	C2	1.484(4)	C11	C12	1.395(5)	C23	C24	1.445(4)	C34	C35	1.486(4)
C1	O1	1.315(4)	C11	N4	1.435(5)	C23	C27	1.356(4)	C34	N6	1.469(4)
C1	O2	1.198(4)	C12	N5	1.491(5)	C24	C25	1.436(4)	C35	N7	1.457(4)
C2	C3	1.436(4)	C13	C14	1.402(6)	C24	O8	1.256(3)	C36	C37	1.372(8)
C2	C6	1.346(4)	C13	N5	1.459(4)	C25	C26	1.390(4)	C36	C41	1.375(6)
C3	C4	1.437(4)	C14	N4	1.472(5)	C25	C30	1.406(4)	C37	C38	1.341(9)
C3	O3	1.262(3)	C15	C16	1.369(5)	C26	N9	1.328(3)	C38	C39	1.352(8)
C4	C5	1.383(4)	C15	C20	1.375(5)	C26	N10	1.381(3)	C40	C41	1.380(5)
C4	C10	1.395(4)	C16	C17	1.370(6)	C27	N10	1.357(3)	C41	C42	1.488(5)
C5	N1	1.385(3)	C17	C18	1.370(6)	C28	C29	1.486(5)	C42	O9	1.227(5)
C5	N2	1.324(3)	C18	C19	1.371(5)	C28	N10	1.476(4)	C42	O10	1.229(5)
C6	N1	1.342(3)	C19	C20	1.372(5)	C30	N8	1.301(3)	C43	C44	1.495(5)
C7	C8	1.498(5)	C20	C21	1.477(5)	C31	N7	1.348(3)	C43	O11	1.236(4)
C7	N1	1.459(3)	C21	O4	1.197(4)	C31	N8	1.356(4)	C43	O12	1.233(4)
C9	N3	1.360(4)	C21	O5	1.309(4)	C31	N9	1.334(3)	C44	C45	1.370(5)
C9	N2	1.338(4)	C22	C23	1.483(4)	C32	C33	1.494(5)	C44	C49	1.375(5)
C9	N4	1.352(4)	C22	O6	1.193(4)	C32	N7	1.449(4)	C45	C46	1.354(6)
N3	C10	1.300(4)	C22	O7	1.323(4)	C33	N6	1.478(4)	C46	C47	1.373(6)

Atom	Atom	Atom	Angle	Atom	Atom	Atom	Angle	Atom	Atom	Atom	Angle	Atom	Atom	Atom	Angle
O1	C1	C2	114.7(3)	C16	C15	C20	119.7(4)	N10	C26	C25	119.4(2)	C45	C44	C43	119.9(3)
O2	C1	C2	124.1(3)	C17	C16	C15	121.5(4)	N10	C27	C23	123.1(2)	C45	C44	C49	119.2(4)
O2	C1	O1	121.2(3)	C18	C17	C16	118.7(4)	N10	C28	C29	112.4(3)	C49	C44	C43	120.9(3)
C3	C2	C1	120.3(3)	C17	C18	C19	120.2(4)	N8	C30	C25	123.5(3)	C46	C45	C44	121.4(4)
C6	C2	C1	119.0(3)	C20	C19	C18	120.9(4)	N7	C31	N8	115.9(2)	C45	C46	C47	119.5(4)
C6	C2	C3	120.7(2)	C15	C20	C19	119.0(3)	N9	C31	N7	117.4(3)	C48	C47	C46	120.2(4)
C4	C3	C2	114.4(3)	C15	C20	C21	122.0(3)	N9	C31	N8	126.6(2)	C47	C48	C49	119.8(4)
O3	C3	C2	123.5(2)	C19	C20	C21	119.0(3)	N7	C32	C33	110.4(3)	C48	C49	C44	120.0(4)
O3	C3	C4	122.1(3)	O4	C21	C20	123.1(3)	N6	C33	C32	109.6(3)	C5	N1	C7	121.0(2)
C5	C4	C3	121.9(2)	O4	C21	O5	122.5(4)	N6	C34	C35	110.5(3)	C6	N1	C5	118.6(2)
C5	C4	C10	115.1(2)	O5	C21	C20	114.3(3)	N7	C35	C34	110.7(3)	C6	N1	C7	120.4(2)
C10	C4	C3	123.0(3)	O6	C22	C23	123.4(3)	C37	C36	C41	119.7(5)	C5	N2	C9	115.1(3)
N1	C5	C4	120.1(2)	O6	C22	O7	121.8(3)	C38	C37	C36	121.1(6)	N3	C10	C4	124.1(3)
N2	C5	C4	123.7(2)	O7	C22	C23	114.8(3)	C37	C38	C39	120.3(6)	C9	N4	C11	123.0(3)
N2	C5	N1	116.2(2)	C24	C23	C22	121.0(3)	C38	C39	C40	120.3(5)	C9	N4	C14	122.0(3)
N1	C6	C2	124.3(3)	C27	C23	C22	118.2(3)	C41	C40	C39	119.0(5)	C11	N4	C14	113.4(3)
N1	C7	C8	113.1(3)	C27	C23	C24	120.8(2)	C36	C41	C42	121.1(4)	C13	N5	C12	112.1(3)
N2	C9	N3	126.8(3)	C25	C24	C23	114.5(3)	C40	C41	C36	119.5(4)	C34	N6	C33	111.9(2)
N2	C9	N4	116.7(3)	O8	C24	C23	122.9(2)	C40	C41	C42	119.3(4)	C31	N7	C32	122.7(2)
N4	C9	N3	116.5(3)	O8	C24	C25	122.7(3)	O9	C42	C41	116.5(4)	C31	N7	C35	123.6(3)
C10	N3	C9	115.1(3)	C26	C25	C24	122.4(2)	O10	C42	C41	118.5(4)	C32	N7	C35	113.7(2)
C12	C11	N4	111.4(4)	C26	C25	C30	115.0(2)	O10	C42	O9	125.0(4)	C30	N8	C31	115.8(2)
C11	C12	N5	112.9(4)	C30	C25	C24	122.6(3)	O11	C43	C44	119.0(3)	C26	N9	C31	115.5(2)
C14	C13	N5	112.8(4)	N9	C26	C25	123.4(2)	O12	C43	C44	119.6(3)	C26	N10	C28	120.2(2)
C13	C14	N4	110.1(4)	N9	C26	N10	117.2(2)	O12	C43	O11	121.4(4)	C27	N10	C26	119.8(2)

Table 3. FT-IR stretching frequencies for OH, CO, NH and CH peaks of PMA, BA, and 4BA.

Compound	ν(OH)$_{COOH}$	ν(CO)$_{COOH}$	ν(CO)$_{pyridone}$	δ(CH)$_{aromatic}$	ν(NH)$_{piperazyl}$
PMA	3459	1617	1640	890	2971
BA	3300-2500	-	-	880	-
4BA	3500	1629	1715	855	2988

3.2. DSC analysis

DSC is a technique used to study thermal transitions in materials. In this case, it was used to determine the melting points of the synthesized molecular salts. The melting points of PMA and 4BA salt were determined by DSC analysis (Figure 3a). The DSC curve for PMA exhibited two peaks: one at 108.1 °C, corresponding to the loss of water from the crystal lattice, and another between 254-259 °C, representing the melting point. The observed difference in the melting point of the 4BA salt compared to PMA suggests interactions between the drug and the conformers, confirming that the melting endotherm associated with the first-order phase transition has disappeared. The presence of only a single endothermic peak at 227.2 °C in Figure 3b for the salt suggests that there is no additional phase transition occurring before melting. This implies a direct transition from the solid state to the liquid state for the molecular salt [33].

3.3. Description of the crystal structure of molecular salt 4BA

A 1:1 molecular salt of PMA and BA was obtained by a solvent evaporation method in methanol water solvent. It crystallized in triclinic, with *P*-1 space group. The symmetric unit contains two PMA molecules and three BA molecules and one water molecule, between which an $R^3_4(10)$ and $R^2_1(4)$ motif (Figure 4a) is formed through four N-H···O (Figure 4a). This primary interaction also include O5-H5···O1S (1.768 Å, 176°) and O1S-H1SA···O 12 (1.82 Å, 176°), resulting in the formation of two S(6). In 4BA, the -COOH group of benzoic acid (BA) is ionized due to the transfer of the proton to the pyridine nitrogen atom of the PMA moiety, while the -OH groups remain unionized. Evidence for proton transfer from the -COOH group (atom O10) to the pyridine ring (atom N5) is provided by the difference in the C-O bond distances: C42-O10 = 1.232(7) Å and C42-O9 = 1.225(6) Å in the carboxylate group, resulting in a ΔD_{CO} value of 0.006 Å. This relatively small ΔD_{CO} value is consistent with what is expected for a carboxylate group [34]. Units were connected via N5-H5A···O11 (1.999 Å, 153.4°) and N6-H6B···O11 (1.767 Å, 177.5°) interactions to form 1D linear chains (Figure 4c). Interestingly, these interactions also had formed a corrugated wave-like structure (Figure 4d) along the *a*-axis. The molecules are linked by the hydrogen bond interaction (Figure 4b) (C27-H27···O2) and C6-H6···O6 propagate in one dimension along the *b* axis, forming ring motif $R^2_2(10)$ and C7-H7B···O6 and C28-H28B···O2 forming two $R^2_1(4)$ motif. These 1D chains arrange in two-dimensional

Table 4. Hydrogen bonds for compound 4BA.

D-H···A	d(D-H), Å	d(H···A), Å	d(D···A), Å	∠ (DHA), °
O1S-H1SA···O 12#6	0.85(5)	1.82(5)	2.665(5)	176(5)
O1S-H1SB···O4 #5	0.87(5)	1.97(5)	2.805(5)	162(6)
O5-H5···O1S#6	0.819(19)	1.768(13)	2.586(5)	176(7)
N5-H5A ···O11 #6	0.900(4)	1.999(4)	2.832(4)	153.4(3)
N5-H5A···O12 #6	0.900(4)	2.228(5)	2.964(5)	138.7(3)
N5-H5B···O10 #6	0.900(4)	1.757(5)	2.643(5)	167.2(4)
N6-H6A ···O9 #6	0.900(4)	1.733(5)	2.614(5)	165.7(4)
N6-H6B···O11#6	0.900(4)	1.767(4)	2.666(4)	177.5(3)
O7-H7···O8 #1	0.82(3)	1.75(2)	2.518(3)	155(3)
C6-H6···O2	0.930(5)	2.492(4)	2.813(4)	100.4(3)
C6-H6···O6 #1	0.930(5)	2.349(4)	3.222(4)	156.3(3)
C7-H7B···O6 #1	0.970(4)	2.496(4)	3.296(4)	139.7(3)
C11-H11B···N2	0.969(8)	2.315(5)	2.745(5)	106.0(4)
C14-H14A···N3	0.970(8)	2.312(5)	2.741(5)	105.9(4)
C27-H27···O2 #2	0.930(5)	2.423(4)	3.300(5)	157.0(3)
C27-H27···O6	0.930(5)	2.471(4)	2.793(4)	100.4(3)
C28-H28B···O2 #2	0.969(5)	2.525(4)	3.401(5)	150.3(3)
C30-H30···N8 #4	0.930(4)	2.467(4)	3.263(4)	143.6(3)
C32-H32B···N9	0.970(5)	2.298(4)	2.745(4)	107.2(3)
C34-H34B···O1 #3	0.970(5)	2.516(4)	3.395(4)	150.6(3)
C35-H35A···N8	0.970(5)	2.298(4)	2.744(4)	107.1(3)
C35-H35A···8 #1	0.970(5)	2.575(4)	3.307(4)	132.3(3)

Symmetry codes: #1) 2+*x*, *y*, -1+*z*; #2) -2+*x*, *y*, 1+*z*; #3) -1+*x*, *y*, 1+*z*; #4) -*x*, 1-*y*, 2-*z*; #5)2-*x*, -*y*, 1-*z*; #6) *x*, *y*, *z*.

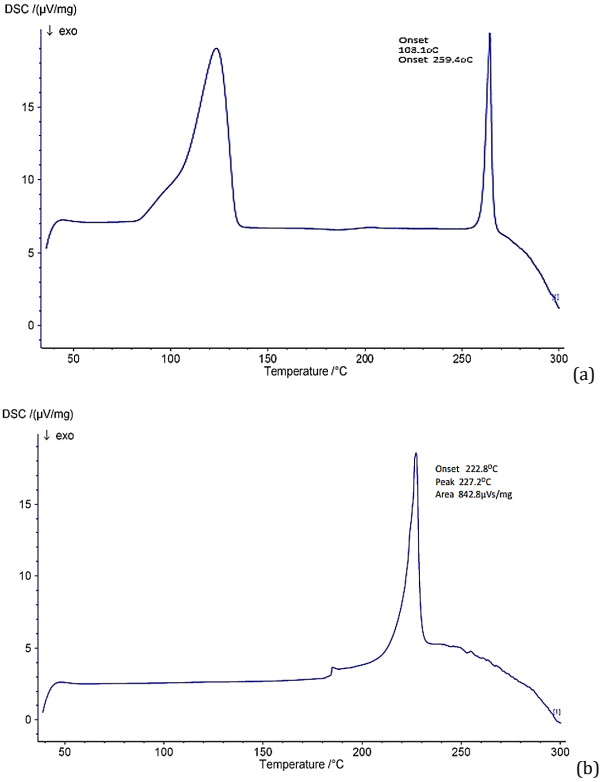

Figure 3. DSC thermograms showing the melting behavior of (a) PMA and (b) 4BA.

(2D) planar structures through N6-H6B···O11 (1.767Å, 177.5°) and O7-H7···O8 (1.75 Å, 155°) interactions (Figure 4c, Table 4). The planar sheets of 4BA are stabilized through π-π stacking interactions of between two pyrimidine molecules with interplanar distance, Cg-Cg distance of 3.790(2), 3.905(2) and 3.665(2) Å, respectively (Figure 4e).

3.4. Salt or co-crystal by ΔpK$_a$

ΔpK_a is a key factor used to differentiate between the formation of co-crystals and salts. If ΔpK_a < 0, a co-crystal is likely formed, while ΔpK_a > 3 indicates salt formation. For values between 0 and 3, the outcome is less predictable and may depend on specific molecular interactions and crystallization conditions; either a salt or a co-crystal may form [35]. The p*K*a values of PMA and BA are 8.57 and 4.20, respectively [36]. As a result, the ΔpK_a values for 4BA is 4.37, suggesting the formation of salts rather than co-crystals.

3.5. Hirshfeld surface analysis

Hirshfeld surface analysis is a valuable tool for finding the significance of hydrogen bonds within crystal systems as well as understanding intramolecular and intermolecular interactions within crystal structures. In the 4BA the Hirshfeld surface, depicted in Figure 5a, showed the surface mapped over a d_{norm} range of -0.5833 to 1.7263 Å.

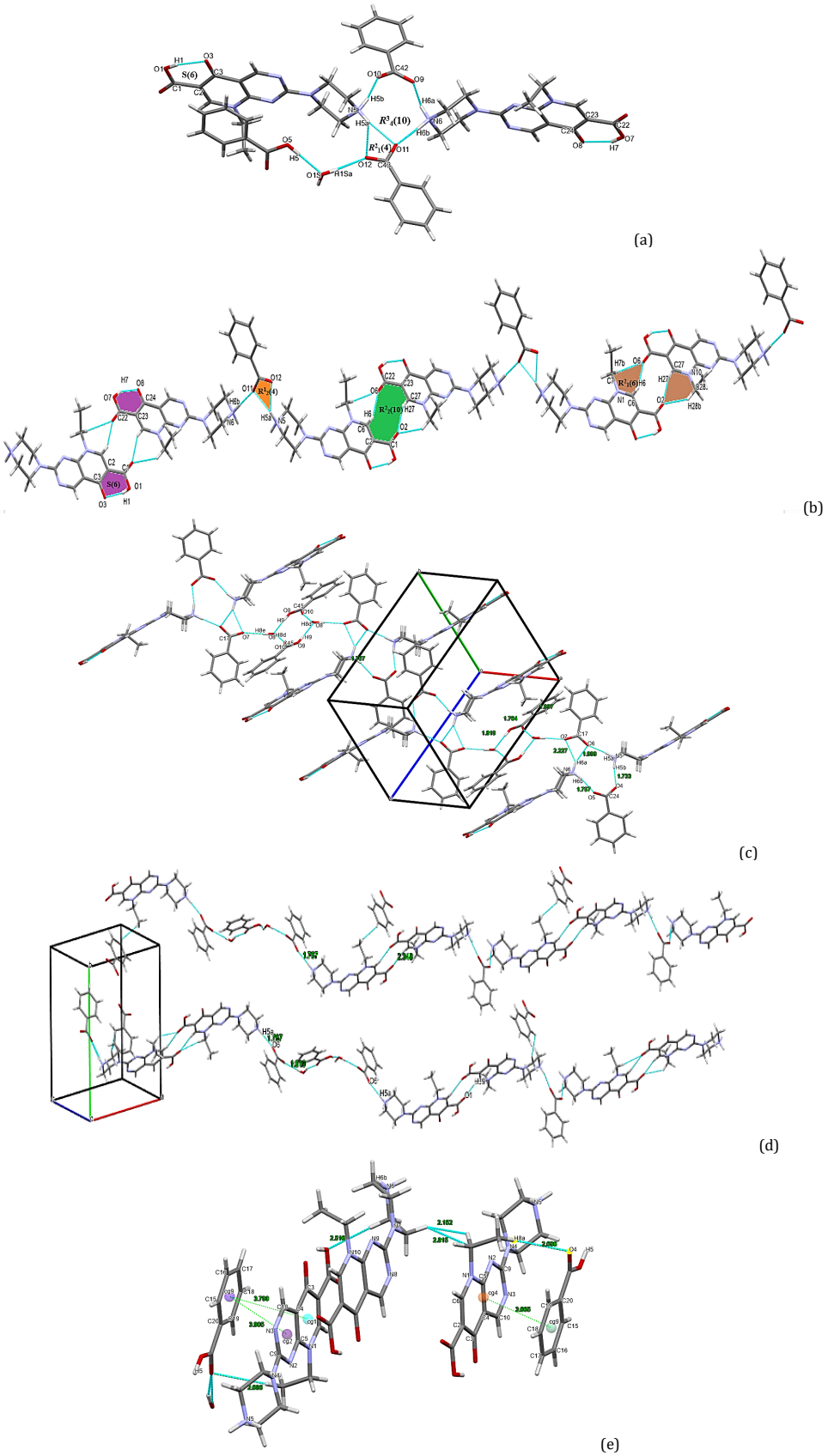

Figure 4. (a) The 4BA salt forms N-H···O and O-H···O hydrogen bonding and are connected by ($R_4^3$10) ring motif. (b) The PMA and BA molecules self-assemble through N-H···O and O-H···O hydrogen bonding interactions, leading to the formation of an extended 2D network. (c) The PMA and BA units form a helical structure connected by a 1D chain of the conformer (d) A wave-like structure is formed through N-H···O and O-H···O hydrogen bonds (e) π-π stacking interactions.

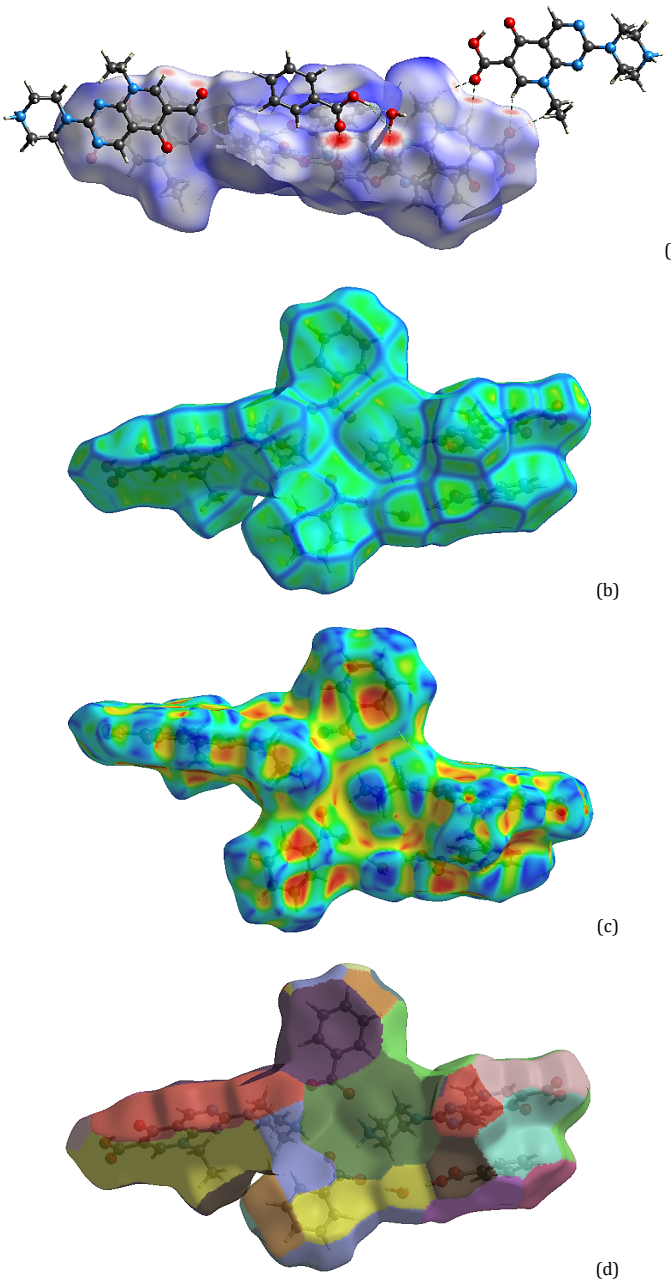

Figure 5. Hirshfeld surfaces of the 4BA (a) The d_{norm} surface of the title compound structure illustrates the intermolecular interactions of N-H···N and C-H···O, (b) Curvedness emphasizing flat areas that contribute to ring interactions in π-stacking, (c) Shape index surface, highlighting π···π interactions, with red and blue triangles within a black ellipse indicating bumps and hollow regions, respectively, evidencing the π···π stacking area and (d) Fragment patches, unique (colored) areas based on atoms external to the Hirshfeld surface, illustrating the closest neighboring molecule.

The regions highlighted in red denote areas associated with hydrogen bonding. Furthermore, Figures 5b and 5c illustrate curvedness and shape index surfaces, respectively, providing information on molecular packing and interactions. The green areas on the curvedness surface signify weaker interactions, while the shape index surface reveals details about the C-H and H···H interactions, highlighting both donor and acceptor regions within the structure. The nearest-neighbour coordination environment of the molecules is identified by the color patches on the Hirshfeld surface, which indicate their proximity to adjacent molecules. Consequently, fragment patches provide an effective method for identifying the nearest neighbor coordination environment of the compounds (Figure 5d).

The selected two-dimensional fingerprint plots for 4BA are shown in Figure 6, which shows all contacts, as well as specific descriptions into H···H, O···H/H···O, and C···H/H···C contacts, with their respective percentage contributions. H···H intermolecular contacts contribute the highest percentage (45.7%), reflecting the abundance of hydrogen from the starting materials. The C···H/H···C and O···H/H···O contacts, attributed to attractive C-H···C and C-H···O hydrogen-bonding interactions, contribute 19.2 and 24.2%, respectively, indicating that these are the dominant stabilizing interactions in this crystal. Additionally, minor contributions from other interatomic contacts to the Hirshfeld surfaces are as follows: N···H/H···N (2.7%), C···N/N···C (2%), O···C/C···O 1.9%), and others 4.3% (Figure 7). In the case of 4BA, the N-H···O hydrogen bonding interactions 24.2% might be due to the rigidity of the carbon skeleton.

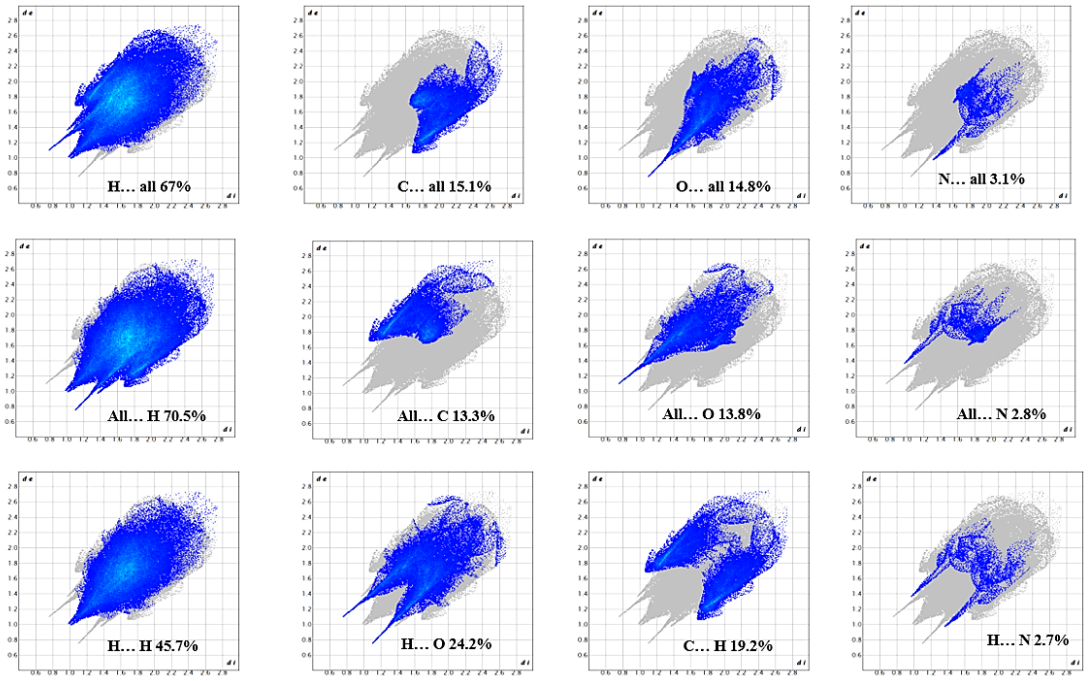

Figure 6. 2D fingerprint plots of 4BA for individual interatomic contacts.

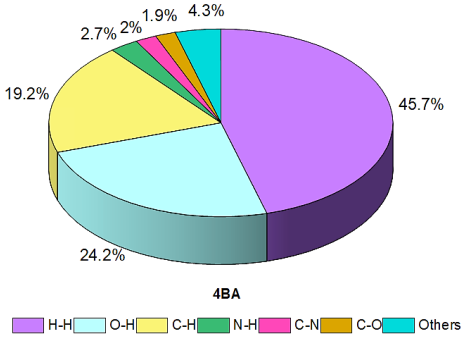

Figure 7. Percentage contribution of each interaction between atoms in 4BA.

The aromatic carboxylic acids used as conformers exhibited an increase in H-H contacts with a higher number of hydrogen donor/acceptor groups present in the carboxylic acids [37,38]. However, the introduction of bulky groups, such as -OCH_3, resulted in a reduction in H-H contacts and longer hydrogen bonding interactions [39]. The increased aromatic character of pipimedic acid and benzoic acid, which were used to prepare the 4BA salt, enhances π···π stacking interactions in the 4BA crystal. The conjugated π-electron systems in these acids promote intermolecular interactions between aromatic rings, leading to greater crystal stability [40]. Similarly, interactions involving carbon atoms [C···All] represent about 15.1% of the total, with d_i values ranging from 0.7534 to 2.7564 Å and de values from 0.7541 to 2.7610 Å. This indicates the ability of carbon atoms to interact across a broad area, drawing atoms closer to the surface because of their lower de values. Similarly, interactions involving outside carbon atoms [All···C] also account for approximately 13.3%. Furthermore, the interactions involving oxygen [O···All] comprise approximately 14.8%, while [All···O] interactions make up 13.4%. Nitrogen interactions [N···All] represent 3.1% and [All···N] interactions constitute 2.8% of the total surface area. These percentages are illustrated in Figure 6, along a selected 2D fingerprint that highlights areas of close contact between inside and outside atoms on the overall surface.

3.6. Enrichment ratios

Hirshfeld surfaces help us break down the crystalline environment to better understand intermolecular interactions by measuring surface areas based on the closest elements. This gives us a quantitative assessment known as Hirshfeld surface contacts. One key measure derived from these contacts is the enrichment ratio (ER). This ratio compares the actual frequency of atom contacts in a crystal with what we would expect if there were no energetic preferences among the interactions. To calculate the enrichment ratio, ER (x, y), for a pair of elements (x,y), we look at how many contacts are actually observed in the crystal compared to the theoretical number of random contacts. If the ratio is greater than one, it means that these two elements are more likely to come into contact with each other in the crystal [41]. On the other hand, a ratio of less than one suggests that they tend to avoid each other. This concept was introduced by Jelsch *et al.* [42]. We can find the enrichment ratios calculated from both Hirshfeld surface contacts and random contacts in Table 5.

Table 5. Enrichment ratios for 4BA.

Contacts	H	C	N	O
H	-	1.05	-	1.38
C	1.05	1.02	2.00	-
N	-	2.00	-	-
O	1.38	-	-	-

Table 6. The various quantum chemical parameters of compound 4BA.

E_{HOMO} (eV)	E_{LUMO} (eV)	Energy gap, ΔE (eV)	Electronegativity, χ (eV)	Global hardness, η (eV)	Global softness, σ (eV^{-1})	Global electrophilicity, ω (eV)
-0.2096	-0.0678	0.1418	0.1387	0.0709	7.0537	0.1357

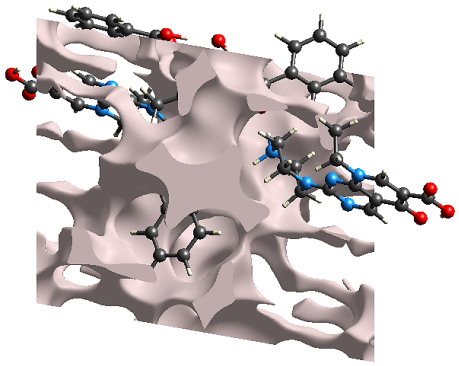

Figure 8. Graphical representation of voids in 4BA.

The analysis reveals that the void space within the crystal accounts for 12.03%, as illustrated in Figure 8. On the contrary, 4BA has a much larger void space, with a void volume of 379.80 Å^3 out of a total volume of 1012.62 Å^3, giving it a void percentage of 37.5%. This result, based on a threshold of 0.002 a.u., suggests that the molecules in the crystal are tightly bound together by non-covalent interactions, indicating that strong intermolecular forces are at work [43].

3.7. Quantum computational studies

The density functional theory (DFT) analysis of the synthesized compounds was performed with Gaussian 09 and Gauss View 6.0 was used for visualization. The structural coordinates of the compound were optimized using the B3LYP/6-31G(d,p) [44] level basis set without symmetry constraints. Using the improved shape, the energies of the compounds and the molecular electrostatic potential map were determined. The HOMO-LUMO energy gap and related reactive characteristics (electronegativity, chemical potential, hardness, softness, and electrophilicity) were estimated using the Koopman's approximation. In computations of quantum chemical properties, frontier molecular orbitals are used to approximate the ionization energy (I) and electron affinity (A) provided by the Koopman's theorem [45]. Frontier molecular orbitals are two types of molecular orbitals: the highest occupied molecular orbital (HOMO) and the lowest unoccupied molecular orbital (LUMO). The chemical stability of the molecule is defined by the difference between its HOMO and LUMO energy levels [46]. The chemical interaction is feasible when this difference is smaller.

The global reactivity descriptors for 4BA provide valuable insight into the reactivity and stability of the compound (Table 6) [47]. These indices, which are derived from the HOMO/LUMO band gap (ΔE), include several key parameters: chemical hardness (η), chemical softness (σ), global electrophilicity (ω), electronegativity (χ), ionization energy (IP), and electron affinity (EA), as detailed in the following (Equations 1-6).

$$EA = -E_{LUMO} \quad (1)$$

$$IP = -E_{HOMO} \quad (2)$$

$$\chi = \frac{IP+EA}{2} \quad (3)$$

$$\eta = \frac{IP-EA}{2} \quad (4)$$

$$\mu = \frac{-E_{HOMO}+E_{LUMO}}{2} \quad (5)$$

$$\sigma = 1/2\eta \quad (6)$$

The ionization potential (IP) (Equation 2) of 0.2096 for this compound indicates a strong electron donating ability, as it requires considerable energy to remove an electron from the highest occupied molecular orbital (HOMO) [48]. On the other hand, the electron affinity (EA) (Equation 1) of 0.0678 suggests that the compound can accept electrons, reflecting the energy change when an electron is added to the lowest unoccupied molecular orbital (LUMO) [49]. The calculated electronegativity (χ) (Equation 3) of 0.1390 indicates a notable tendency to attract electrons [50]. With a chemical hardness (η) (Equation 4) of 0.0709, the compound shows stability against changes in its electronic structure, while a chemical potential (μ) (Equation 5) of -0.1390 suggests a low tendency to exchange electrons with its surroundings. The softness (σ) value of 7.0537 (Equation 6) implies that the compound is relatively hard, which means that it resists the deformation of its electron cloud [51]. Furthermore, a global electrophilicity index (ω) of 0.1356 indicates significant electrophilic character, suggesting a strong tendency to accept electrons [52].

Density functional theory (DFT) calculations, using the B3LYP/6-31G(d,p) basis set, were used to compute the optimized geometry and the molecular electrostatic potential (MEP) (Figure 9) of the synthesized compounds. The MEP is particularly useful for identifying regions that favor intramolecular and intermolecular interactions. The red and yellow regions indicate negative electrostatic potentials, while the blue region indicates positive potential, and the green region indicates a neutral potential area.

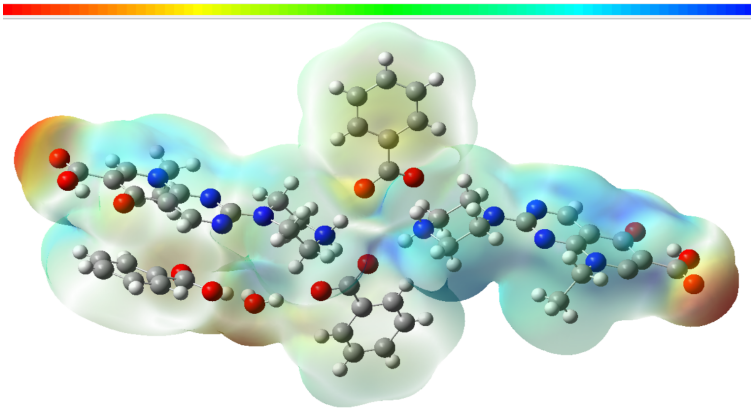

Figure 9. Optimized structure with molecular electrostatic potential of compound 4BA.

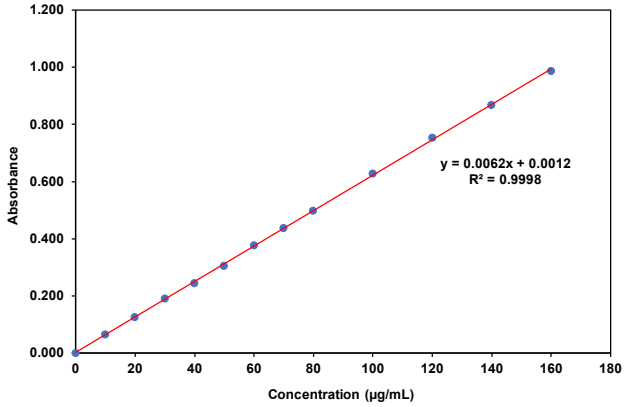

Figure 10. Calibration curve of PMA in PBS.

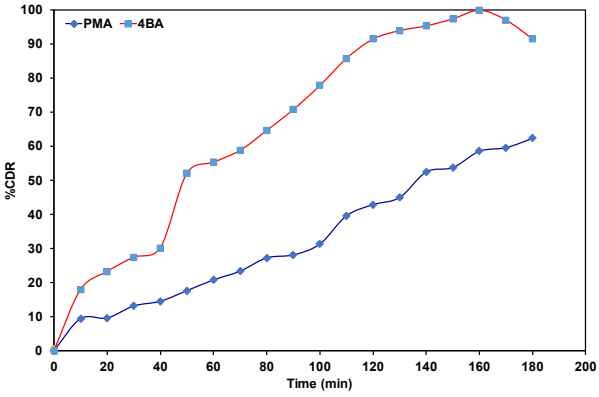

Figure 11. %CDR profiles of PMA and its molecular salt 4BA.

The DFT-calculated Mulliken's atomic charges reveal the charge distribution across individual atoms [53]. The HOMO, LUMO, and the energy gap (ΔE) of the isolated compounds, presented in Table 6, show that the compound has a low energy gap (ΔE), suggesting high chemical reactivity and significant intramolecular charge transfer from the electron-donor (HOMO) to the electron-acceptor (LUMO) groups.

3.8. Dissolution study

The calibration curve (Figure 10) of PMA in PBS was used to determine drug release during *in vitro* release measurements. Figure 11 shows that the study investigated the cumulative percentage of drug release (%CDR) of drug (PMA) and its salt over a period of 180 minutes. The initial release is observed within the first 10 minutes in the 4BA. This could be attributed to drug molecules present on the surface of the formulation that dissolve easily in the surrounding medium [48].

In this study, we have also examined the salts that were prepared and analyzed in our previous research, as described in the reference [54]. This continuity ensures a clear understanding of the materials used and their relevance to our current findings. Our previous study [54] focused on the structural characterization of the molecular salts 1OA (oxalic acid) 2SA (salicylic acid), and 3BS (*p*-toluene sulfonic monohydrate).

Table 7. MIC analysis of PMA and its molecular salts (1OA, 2SA, 3BS and 4BA).

Names	MIC (µg/mL)				
	PMA	4BA	3BS	2SA	1OA
Escherichia coli	>256	>256	>256	>256	>256
Mycobacterium smegmatis	>256	>256	>256	>256	>256
Klebsiella pneumoniae	64	>256	64	64	64
Staphylococcus aureus	16	64	64	64	>256
Pseudomonas aeruginosa	128	32	32	64	128
Acinetobacter baumannii	64	256	256	256	256

Table 8. Biofilm formation analysis of PMA and its molecular salts (1OA, 2SA, 3BS, and 4BA).

Concentration, µg/mL	Biofilm formation (%)				
	PMA	4BA	3BS	2SA	1OA
16	100	58	66	75	22
32	40	15	27	27	35

In this study, we further investigated their dissolution profiles along with 4BA to compare their drug release behaviour. The extent of drug release varied among these salts, with PMA showing the lowest initial release at 9.41% in the first 10 minutes. On the contrary, the molecular salts exhibited higher initial release rates: 1OA (19.39%), 2SA (14.75%), 3BS (17.94%), and 4BA (17.94%). This variation in release rates suggests that salt formulations provide a more accessible drug distribution on their surfaces, enhancing dissolution compared to that of pure PMA.

Comparison of %CDR for PMA and its molecular salts (1OA, 2SA, 3BS, and 4BA) reveals substantial differences in their dissolution profiles, highlighting the impact of salt formation on drug release [54]. PMA exhibits a slower, sustained release, reaching a maximum %CDR of 62.43% at 180 minutes, while its molecular salts demonstrate significantly enhanced dissolution. This improvement is attributed to structural modifications introduced by salt formation that improve solubility, wettability, and molecular interactions with the dissolution medium. In our previous study [55], the structural characterization of 1OA, 2SA, and 3BS provided information on their molecular arrangement, hydrogen bonding patterns, and potential for solubility enhancement. However, this study is the first to assess their dissolution behavior, confirming that all salts exhibit superior drug release compared to that of PMA. Among them, 1OA and 3BS show the highest %CDR values at later time points, suggesting a more sustained release profile. 4BA, however, showed the most rapid dissolution, reaching 105.2% at 160 minutes before slightly decreasing to 96.77% at 180 minutes. The difference is observed at 50 minutes, where 4BA's %CDR (52.16%) is nearly threefold that of PMA (17.64%), providing strong indication that salt formation enhances drug solubility and bioavailability. The observed trend aligns with the literature reports on salt formation as an effective strategy for solubility enhancement. Studies on structurally similar carboxylate and benzoate salts suggest that increased ionization, altered crystal packing, and improved intermolecular interactions contribute to accelerated dissolution. The rapid release of the drug observed for 4BA may be attributed to its enhanced molecular interactions, increased surface wettability, and reduced lattice energy, facilitating faster drug diffusion into the dissolution medium [55].

3.9. Antibacterial activity analysis of PMA and its molecular salts (1OA, 2SA, 3BS, and 4BA)

MIC values were determined for the PMA salts, designated as 2SA, 3BS and 1OA which were reported earlier [54] along with 4BA, against *Escherichia coli*, *Mycobacterium smegmatis*, *Klebsiella pneumoniae*, *Staphylococcus aureus*, *Pseudomonas aeruginosa*, and *Acinetobacter baumannii*. Among the organisms evaluated, relative to PMA, its salts (4BA, 3BS, and 2SA) showed (Table 7) a stronger antibacterial effect against *Pseudomonas aeruginosa*. For other organisms, PMA had a comparable or better effect in comparison to salts of PMA. Interestingly, the MIC of PMA was lowest against methicillin-resistant *Staphylococcus aureus* (16 µg/mL) although the salts were not more effective relative to PMA.

3.9.1. Biofilm assay

The ability of biofilm formation was assessed against the ESKAPE pathogens. Among them, the PMA salts caused significant inhibition of *P. aeruginosa* biofilms BA salt at 32 µg/mL was most effective and caused 85% inhibition of PA biofilms, followed by BS and SA salts that caused 73% biofilm inhibition. Relatively, PMA at 32 µg/mL caused 60 % biofilm inhibition. Therefore, 4BA and 3BS salts of PMA possessed both a significant antibacterial and antibiofilm effect relative to the PMA (Table 8). The enhanced antibacterial and antibiofilm activity proves that improved salts of PMA could serve as a strong antibiofilm agent. Since the concentrations at which these improved salts exert the antibacterial and antibiofilm effect are similar, it is likely that the antibiofilm effect could be mediated by the antibacterial effect, which remains to be confirmed by live/dead staining in future studies [56].

4. Conclusions

In this study, we prepared and analyzed a molecular salt of the antibacterial drug pipimedic acid (PMA) using a range of techniques, including single crystal and powder X-ray diffraction, Hirshfeld surface analysis, FT-IR spectroscopy, and differential scanning calorimetry. Our findings revealed that the compound 4BA is formed through the interaction of acid and pyridine hetero synthons. We also evaluated the intermolecular interactions within all complexes using Hirshfeld surface analysis and 2D fingerprint plots. DFT analysis highlighted the significance of π-π interactions in the solid state, which are essential for understanding how molecules pack together. These interactions are typically energetically favourable, largely due to their strong electrostatic contributions, and are key to elucidating the solid-state structure of 4BA. The results of FT-IR spectroscopy confirmed the successful formation of the molecular salt, while the DSC showed a distinct endothermic peak at 227.2 °C for BA, indicating its well-defined crystalline nature and purity. The findings of the MEP and Mulliken population analysis were consistent, highlighting important regions that are chemically active. DFT calculations yielded values of chemical hardness (η) at 0.0709 eV and chemical softness (σ) at 7.0537 eV, suggesting that this compound is relatively hard and has a significant propensity to engage in chemical reactions. The energy gap between the HOMO and the LUMO was calculated to be 0.1418 eV, reinforcing the idea that the molecule is indeed hard. From the Hirshfeld surface analysis, it was determined that the main contributions to the crystal packing arose from H···H interactions (45.7), Cl···H/H···Cl interactions (24.2%), and C···H/H···C interactions

(19.2%). Additionally, the calculated global reactivity parameters confirmed the stability of 4BA, as shown by the comparisons of their HOMO/LUMO and optical gaps. The compound exhibited a high degree of electronegativity (χ, eV) and global electrophilicity (ω, eV), suggesting promising bioactivity. These conclusions were further supported by antibacterial assays, in which 4BA showed a notable 85% inhibition of biofilm formation. The dissolution study clearly indicates that 4BA exhibits a rapid and higher drug release profile compared to PMA, with a three-fold increase observed at 50 minutes, highlighting the potential of 4BA for faster therapeutic action.

Acknowledgements

The SJC would like to express their sincere appreciation to Sri Sathya Sai University for Human Excellence, Kalaburagi, for the support in facilitating this research.

Supporting information

CCDC-2168989 contains the supplementary crystallographic data for this paper. These data can be obtained free of charge via www.ccdc.cam.ac.uk/data_request/cif, or by e-mailing data_request@ccdc.cam.ac.uk, or by contacting The Cambridge Crystallographic Data Centre, 12 Union Road, Cambridge CB2 1EZ, UK; fax: +44(0)1223-336033.

Disclosure statement

Conflict of interest: The authors declare that they have no conflict of interest.
Ethical approval: All ethical guidelines have been adhered to.
Sample availability: Samples of the compounds are available from the author.

CRediT authorship contribution statement

Conceptualization: Kamalakaran Anand Solomon; Methodology: Shwetha Jayapura Chandrashekar; Software: Rajalakshmanan Eswaramoorthy; Formal Analysis: Shwetha Jayapura Chandrashekar; Data Curation: Rajalakshmanan Eswaramoorthy; Writing - Original Draft: Shwetha Jayapura Chandrashekar; Writing - Review and Editing: Shwetha Jayapura Chandrashekar, Kamalakaran Anand Solomon; Supervision: Kamalakaran Anand Solomon.

ORCID and Email

Shwetha Jayapura Chandrashekar
shwetha.jc@gmail.com
https://orcid.org/0000-0002-3262-7583
Rajalakshmanan Eswaramoorthy
rajalakshmanan.e@gmail.com
https://orcid.org/0000-0002-8331-2100
Kamalakaran Anand Solomon
anand.dcb@gmail.com
https://orcid.org/0000-0003-4677-2340

References

[1]. Shimizu, M.; Takase, Y.; Nakamura, S.; Katae, H.; Minami, A.; Nakata, K.; Inoue, S.; Ishiyama, M.; Kubo, Y. Pipemidic Acid, a New Antibacterial Agent Active Against *Pseudomonas aeruginosa* In Vitro Properties. *Antimicrob Agents Chemother* **1975**, *8* (2), 132–138.
[2]. Fernandes, P. B. Mode of Action, and In Vitro and *In Vivo* Activities of the Fluoroquinolones. *The Journal of Clinical Pharma* **1988**, *28* (2), 156–168.
[3]. Zhang, Y.; Duan, Y.; Su, J.; Liu, L.; Feng, Y.; Wu, L.; Zhang, L.; Zhang, Y.; Zou, D.; Liu, Y. Inspiration for revival of old drugs: improving solubility and avoiding hygroscopicity of pipemidic acid by forming two pharmaceutical salts based on charge-assisted hydrogen bond recognitions. *New J. Chem.* **2021**, *45* (42), 19704–19713.
[4]. Zhang, X.; Chen, J.; Hu, J.; Liu, M.; Cai, Z.; Xu, Y.; Sun, B. The solubilities of benzoic acid and its nitro-derivatives, 3-nitro and 3,5-dinitrobenzoic acids. *J. Chem. Res.* **2021**, *45* (11-12), 1100–1106.
[5]. Jouyban, A.; Rahimpour, E.; E. Acree Jr., W. Further Analysis on Solubility Measurement and Thermodynamic Modeling of Benzoic Acid in Monosolvents and Binary Mixtures. *Pharm. Sci.* **2019**, *25* (2), 165–170.
[6]. Sopyan, I.; Layyareza, R. T.; Megantara, S.; Marvita, S. S. Carvedilol solubility enhancement by multicomponent crystallization with coformers of benzoic acid, isonicotinamide, and saccharin. *Pharmacia* **2023**, *70* (2), 283–290.
[7]. Mannava, M. K.; Garai, A.; Bommaka, M. K.; Solomon, K. A.; Nangia, A. K. Solubility and permeability enhancement of BCS class IV drug ribociclib through cocrystallization. *CrystEngComm* **2022**, *24* (45), 7915–7923.
[8]. Florindo, C.; Costa, A.; Matos, C.; Nunes, S. L.; Matias, A. N.; Duarte, C. M.; Rebelo, L. P.; Branco, L. C.; Marrucho, I. M. Novel organic salts based on fluoroquinolone drugs: Synthesis, bioavailability and toxicological profiles. *Int. J. Pharm.* **2014**, *469* (1), 179–189.
[9]. Khadka, P.; Ro, J.; Kim, H.; Kim, I.; Kim, J. T.; Kim, H.; Cho, J. M.; Yun, G.; Lee, J. Pharmaceutical particle technologies: An approach to improve drug solubility, dissolution and bioavailability. *Asian J. Pharm. Sci.* **2014**, *9* (6), 304–316.
[10]. Yang, J.; Yin, L.; Gong, X.; Sinditskii, V. P.; Zhang, J. Origins of Salt Formation and Cocrystallization: A Combined Experimental and Theoretical Study. *Cryst. Growth amp; Des.* **2020**, *20* (9), 5834–5842.
[11]. Berry, D. J.; Steed, J. W. Pharmaceutical cocrystals, salts and multicomponent systems; intermolecular interactions and property based design. *Adv. Drug Deliv. Rev.* **2017**, *117*, 3–24.
[12]. Gupta, D.; Bhatia, D.; Dave, V.; Sutariya, V.; Varghese Gupta, S. Salts of Therapeutic Agents: Chemical, Physicochemical, and Biological Considerations. *Molecules* **2018**, *23* (7), 1719.
[13]. Del Olmo, A.; Calzada, J.; Nuñez, M. Benzoic acid and its derivatives as naturally occurring compounds in foods and as additives: Uses, exposure, and controversy. *Crit. Rev. Food Sci. Nutr.* **2017**, *57*, 3084–3103.
[14]. Cerreia Vioglio, P.; Chierotti, M. R.; Gobetto, R. Pharmaceutical aspects of salt and cocrystal forms of APIs and characterization challenges. *Adv. Drug Deliv. Rev.* **2017**, *117*, 86–110.
[15]. Rajkumar, M.; Chandramohan, A. Synthesis, growth, structural characterization and biological investigation of hydrogen bonded organic molecular salt: N, N-diethylanilinium-5-sulphosalicylate. *J. Mol. Struct.* **2019**, *1192*, 122–131.
[16]. Karthammaiah, G. N.; Rao Amaraneni, S.; Solomon, A. K. Co-crystal of nadifloxacin with oxalic acid. *Acta Crystallogr E. Cryst Commun* **2023**, *79* (4), 319–322.
[17]. Mashhadi, S. M.; Yufit, D.; Liu, H.; Hodgkinson, P.; Yunus, U. Synthesis and structural characterization of cocrystals of isoniazid and cinnamic acid derivatives. *J. Mol. Struct.* **2020**, *1219*, 128621.
[18]. Chaves Júnior, J. V.; dos Santos, J. A.; Lins, T. B.; de Araújo Batista, R. S.; de Lima Neto, S. A.; de Santana Oliveira, A.; Nogueira, F. H.; Gomes, A. P.; de Sousa, D. P.; de Souza, F. S.; Aragão, C. F. A New Ferulic Acid–Nicotinamide Cocrystal With Improved Solubility and Dissolution Performance. *J. Pharm. Sci.* **2020**, *109* (3), 1330–1337.
[19]. Anand Solomon, K. Molecular modelling and drug design; Mjp Publisher, 2023.
[20]. Karki, S.; Friščić, T.; Fábián, L.; Laity, P. R.; Day, G. M.; Jones, W. Improving Mechanical Properties of Crystalline Solids by Cocrystal Formation: New Compressible Forms of Paracetamol. *Adv. Mater.* **2009**, *21* (38-39), 3905–3909.
[21]. Champa, R.; Vishnumurthy, K.; Bodke, Y. D.; Bhojya Naik, H.; Pushpavathi, I.; Meghana, P.; Kadam, P. R. Synthesis, characterization, and biological investigations of potentially bioactive heterocyclic compounds containing benzimidazole nucleus. *Results Chem.* **2023**, *6*, 101018.
[22]. Mannava, M. K.; Garai, A.; Bommaka, M. K.; Solomon, K. A.; Nangia, A. K. Solubility and permeability enhancement of BCS class IV drug ribociclib through cocrystallization. *CrystEngComm* **2022**, *24* (45), 7915–7923.
[23]. Dolomanov, O. V.; Bourhis, L. J.; Gildea, R. J.; Howard, J. A.; Puschmann, H. *OLEX2*: a complete structure solution, refinement and analysis program. *J. Appl Crystallogr* **2009**, *42* (2), 339–341.
[24]. Spackman, P. R.; Turner, M. J.; McKinnon, J. J.; Wolff, S. K.; Grimwood, D. J.; Jayatilaka, D.; Spackman, M. A. *CrystalExplorer*: a program for Hirshfeld surface analysis, visualization and quantitative analysis of molecular crystals. *J. Appl Crystallogr* **2021**, *54* (3), 1006–1011.
[25]. Puchkov, S. V.; Nepomnyashchikh, Y. V. Evaluation of the Reactivity of Cyclohexanone CH Bonds in Reactions with tert-Butylperoxy Radical by Quantum Chemical Methods. *Kinet Catal* **2021**, *62* (4), 479–487.
[26]. Srikanth, K. E.; Veeraiah, A.; Pooventhiran, T.; Thomas, R.; Solomon, K. A.; Soma Raju, C.; Latha, J. N. Detailed molecular structure (XRD), conformational search, spectroscopic characterization (IR, Raman, UV, fluorescence), quantum mechanical properties and bioactivity prediction of a pyrrole analogue. *Heliyon* **2020**, *6* (6), e04106.
[27]. Stuart, J. G.; Jebaraj, J. W. Synthesis, characterisation, in silico molecular docking and DFT studies of 2,6-bis(4-hydroxy-3-methoxyphenyl)-3,5-dimethylpiperidin-4-one. *Indian J. Chem.* **2023**, *62*, 1061–1080 https://doi.org/10.56042/ijc.v62i10.6186
[28]. Mišura, O.; Kodrin, I.; Borovina, M.; Pisačić, M.; De Silva, V.; Aakeröy, C. B.; Đaković, M. Exploring the Co-Crystallization Landscape of One-Dimensional Coordination Polymers Using a Molecular Electrostatic

Potential-Driven Approach. *Cryst. Growth amp; Des.* **2023**, *23* (10), 7198–7206.
[29]. Manin, A. N.; Drozd, K. V.; Churakov, A. V.; Perlovich, G. L. Hydrogen Bond Donor/Acceptor Ratios of the Coformers: Do They Really Matter for the Prediction of Molecular Packing in Cocrystals? The Case of Benzamide Derivatives with Dicarboxylic Acids. *Cryst. Growth amp; Des.* **2018**, *18* (9), 5254–5269.
[30]. Yang, L.; Tao, D.; Yang, X.; Li, Y.; Guo, Y. Synthesis, characterization, and antibacterial activities of some rare Earth metal complexes of pipemidic acid. *Chem. Pharm. Bull. (Tokyo)* **2003**, *51*, 494–498.
[31]. Siddiqi, A. Z.; Mirza, A. Z. Synthesis, characterization, and antibacterial studies of pipemidic acid metal complexes. *Futur J. Pharm Sci* **2021**, *7* (1), https://doi.org/10.1186/s43094–021–00301–8.
[32]. Rodríguez-Rodríguez, W. A.; Colón, J.; Guzmán, R.; Rivera, H.; Santiago-Berríos, M. B. Synthesis, characterization and electrochemical characterization of lead selenide sub-micron particles capped with a benzoate ligand and prepared at different temperatures. *Mater. Res. Express* **2014**, *1* (3), 035906.
[33]. Hariprasad, V. M.; Nechipadappu, S. K.; Trivedi, D. R. Cocrystals of Ethenzamide: Study of Structural and Physicochemical Properties. *Cryst. Growth amp; Des.* **2016**, *16* (8), 4473–4481.
[34]. Solomon, K. A.; Blacque, O.; Venkatnarayan, R. Molecular salts of 2,6-dihydroxybenzoic acid (2,6-DHB) with N-heterocycles: Crystal structures, spectral properties and Hirshfeld surface analysis. *J. Mol. Struct.* **2017**, *1134*, 190–198.
[35]. Cruz-Cabeza, A. J. Acid–base crystalline complexes and the pKa rule. *CrystEngComm* **2012**, *14* (20), 6362–6365.
[36]. Seaton, C. C.; Parkin, A. Making benzamide cocrystals with benzoic acids: The influence of chemical structure. *Cryst. Growth Des.* **2011**, *11*, 1502–1511.
[37]. Desiraju, G. R. Supramolecular Synthons in Crystal Engineering—A New Organic Synthesis. *Angew. Chem. Int. Ed. Engl.* **1995**, *34* (21), 2311–2327.
[38]. Braga, D.; Grepioni, F.; Maini, L. ChemInform Abstract: The Growing World of Crystal Forms. *ChemInform* **2010**, *41* (47), 6232–6242 https://doi.org/10.1002/chin.201047264.
[39]. Luo, Y.; Sun, B. Pharmaceutical Co-Crystals of Pyrazinecarboxamide (PZA) with Various Carboxylic Acids: Crystallography, Hirshfeld Surfaces, and Dissolution Study. *Cryst. Growth amp; Des.* **2013**, *13* (5), 2098–2106.
[40]. MacGillivray, L. R. Organic Synthesis in the Solid State via Hydrogen-Bond-Driven Self-Assembly. *J. Org. Chem.* **2008**, *73* (9), 3311–3317.
[41]. Siegfried, A. M.; Arman, H. D.; Kobra, K.; Liu, K.; Peloquin, A. J.; McMillen, C. D.; Hanks, T.; Pennington, W. T. Phosphorus···Iodine Halogen Bonding in Cocrystals of Bis(diphenylphosphino)ethane (dppe) and *p*-Diiodotetrafluorobenzene (*p*-F_4DIB). *Cryst. Growth amp; Des.* **2020**, *20* (11), 7460–7469.
[42]. Amarne, H.; Helal, W.; Taher, D.; Korb, M.; Al-Hunaiti, A. Crystal structure, Hirshfeld surface analysis and contact enrichment ratios of 5,5-dimethyl-2-(2,4,6-tris(trifluoromethyl)phenyl)-1,3,2-dioxaborinane. *Mol. Cryst. Liq. Cryst.* **2022**, *743*, 77–88.
[43]. Irrou, E.; Elmachkouri, Y. A.; Oubella, A.; Ouchtak, H.; Dalbouha, S.; Mague, J. T.; Hökelek, T.; El Ghayati, L.; Sebbar, N. K.; Taha, M. L. Crystal structure determination, Hirshfeld surface, crystal void, intermolecular interaction energy analyses, as well as DFT and energy framework calculations of 2-(4-oxo-4,5-dihydro-1*H*-pyrazolo[3,4-*d*]pyrimidin-1-yl)acetic acid. *Acta Crystallogr E. Cryst Commun* **2022**, *78* (9), 953–960.
[44]. Sangeetha, M.; Mathammal, R. Establishment of the structural and enhanced physicochemical properties of the cocrystal-2-benzyl amino pyridine with oxalic acid. *J. Mol. Struct.* **2017**, *1143*, 192–203.
[45]. Üstün, E.; Şahin, N. Density Functional Theory and Molecular Docking Analysis of Newly Synthesized and Characterized Benzimidazolium Salts. *Ordu Universitesi Bilim ve Teknol. Derg.* **2022**, *12* (1), 52–63.
[46]. Phetmung, H.; Musikapong, K.; Srichana, T. Thermal analysis, structure, spectroscopy and DFT calculations of a pharmaceutical cocrystal of salicylic acid and salicylamide. *J. Therm Anal Calorim* **2019**, *138* (2), 1207–1220.
[47]. Pandey, J.; Prajapati, P.; Shimpi, M. R.; Tandon, P.; Velaga, S. P.; Srivastava, A.; Sinha, K. Studies of molecular structure, hydrogen bonding and chemical activity of a nitrofurantoin-l-proline cocrystal: a combined spectroscopic and quantum chemical approach. *RSC. Adv.* **2016**, *6* (78), 74135–74154.
[48]. Abbas, F.; Mohammadi, M. D.; Louis, H.; Amodu, I. O.; Charlie, D. E.; Gber, T. E. Design of new bithieno thiophene (BTTI) central core-based small molecules as efficient hole transport materials for perovskite solar cells and donor materials for organic solar cells. *Mater. Sci. Eng.: B* **2023**, *291*, 116392.
[49]. Bakheit, A. H.; Alkahtani, H. M. Integrated Structural, Functional, and ADMET Analysis of 2-Methoxy-4,6-diphenylnicotinonitrile: The Convergence of X-ray Diffraction, Molecular Docking, Dynamic Simulations, and Advanced Computational Insights. *Molecules* **2023**, *28* (19), 6859.
[50]. Bouallag, S.; Mougari, A.; Zabat, M.; Belayadi, A. Computational study of transition metal coordinated polyaniline: A first principle investigation into tuning the electronic properties of the resulting hybrid material. *Phys. B: Condens. Matter* **2024**, *695*, 416597.
[51]. Agwamba, E. C.; Benjamin, I.; Louis, H.; Udoikono, A. D.; Igbalagh, A. T.; Egemonye, T. C.; Adeyinka, A. S. Antitubercolusic Potential of Amino-(formylphenyl) Diazenyl-Hydroxyl and Nitro-Substituted Naphthalene-Sulfonic Acid Derivatives: Experimental and Theoretical Investigations. *Chem. Afr.* **2022**, *5* (5), 1451–1467.
[52]. Yan, Y.; Wang, X.; Zhang, Y.; Wang, P.; Zhang, J. Theoretical evaluation of inhibition performance of purine corrosion inhibitors. *Mol. Simul.* **2013**, *39* (13), 1034–1041.
[53]. Phetmung, H.; Musikapong, K.; Srichana, T. Thermal analysis, structure, spectroscopy and DFT calculations of a pharmaceutical cocrystal of salicylic acid and salicylamide. *J. Therm. Anal. Calorim.* **2019**, *138*, 1207–1220.
[54]. Shwetha, J. C.; Sharma, A.; Solomon, K. A. Molecular salts of pipemedic acid and crystal structure, spectral properties, and Hirshfeld surface analysis. *J. Iran Chem. Soc.* **2023**, *20* (12), 3161–3176.
[55]. Nyamba, I.; Sombié, C. B.; Yabré, M.; Zimé-Diawara, H.; Yaméogo, J.; Ouédraogo, S.; Lechanteur, A.; Semdé, R.; Evrard, B. Pharmaceutical approaches for enhancing solubility and oral bioavailability of poorly soluble drugs. *Eur. J. Pharm. Biopharm.* **2024**, *204*, 114513.
[56]. Lekhan, A.; Fiore, C.; Shemchuk, O.; Grepioni, F.; Braga, D.; Turner, R. J. Comparison of Antimicrobial and Antibiofilm Activity of Proflavine Co-crystallized with Silver, Copper, Zinc, and Gallium Salts. *ACS. Appl. Bio Mater.* **2022**, *5* (9), 4203–4212.

Copyright © 2025 by Authors. This work is published and licensed by Atlanta Publishing House LLC, Atlanta, GA, USA. The full terms of this license are available at https://www.eurjchem.com/index.php/eurjchem/terms and incorporate the Creative Commons Attribution-Non Commercial (CC BY NC) (International, v4.0) License (http://creativecommons.org/licenses/by-nc/4.0). By accessing the work, you hereby accept the Terms. This is an open access article distributed under the terms and conditions of the CC BY NC License, which permits unrestricted non-commercial use, distribution, and reproduction in any medium, provided the original work is properly cited without any further permission from Atlanta Publishing House LLC (European Journal of Chemistry). No use, distribution, or reproduction is permitted which does not comply with these terms. Permissions for commercial use of this work beyond the scope of the License (https://www.eurjchem.com/index.php/eurjchem/terms) are administered by Atlanta Publishing House LLC (European Journal of Chemistry).